Text S1. Power Series fits to long-term changes: Derivation of LTC(t)

The role of LTC(t) in Equation 1 is to quantify the average long-term changes that underlie the monthly mean ozone time series. This function is subtracted from the time series to detrend the monthly means, which isolates seasonal variations from longer-term changes. The detrended monthly means are then used as input for the Fourier Transform analysis, which quantifies the seasonal cycle; the Fourier analysis is discussed in detail in section S2.

 The physical basis underlying the derivation of LTC(t) is that the average atmospheric composition is continuous over time; across long time scales, the atmosphere does not undergo abrupt, discontinuous changes. Therefore, a power series, i.e., a least-squares regression fit to a polynomial, is an effective functional form to detrend the time series (as opposed to, e.g., a piecewise discontinuous function such as sequential straight line segments), because a power series can effectively

10 approximate any continuous function. When implementing a polynomial fit, a decision must be made regarding the number of polynomial terms to use in the fit. In principle, any function can be exactly fit with a power series of infinite terms; for our purposes it is important to choose a number of polynomial terms that effectively quantifies the long-term changes without over-fitting the time series or including statistically insignificant terms. Figure S1 shows an example monthly mean ozone time series with several LTC(t) functions derived from polynomial fits with between 2 and 12 terms. The polynomial

15 parameters in these fits are statistically significant at the 95% confidence limit (i.e., the confidence interval does not include 0). Therefore, the LTC(t) can be approximated by a polynomial up to at least 11th-order. Table S1 shows that all of these fits effectively detrend the time series, giving seasonal cycle parameters that agree within their statistical confidence limits, regardless of the number of polynomial terms. Therefore, fits with as few as 2 polynomial terms and as many as 12 polynomial terms can effectively detrend the monthly mean time series. This result shows that the long-term change and the

20 seasonal cycle of ozone in monthly mean time series approximate orthogonal functions, mathematically speaking.

 As is apparent in Figure S1, there is negligible difference between LTC(t) fits with 5 polynomial terms (indicated by the green trace) and 12 polynomial terms (indicated by the purple trace). There is a small, gradual improvement in the percentage of variance captured by the fit to Equation (5) and in the confidence limits of the derived parameters as the number of polynomial terms increases. In our analysis, we choose to use a 5-term, 4th-order polynomial for LTC(t). Figure

25 S1 and Table S1 show that this choice, although arbitrary, returns nearly optimal confidence limits for seasonal cycle parameters without the complexity of additional polynomial terms.

 Figure S2 shows a comparison of LTC(t) functions derived from six model simulations (shown in colors as indicated in the legend) and observations (shown in black) at Hohenpeissenberg, where the measurement record is longest. This comparison highlights the differences in long-term average ozone concentrations between model simulations, and between

30 models and measurements. The models, except for GISS-E2-1-H, do not reproduce the strong curvature in long-term average ozone concentrations in later years. However, three of the six models (CESM2-WACCM, GFDL-ESM4, and MRI-ESM2-0) do accurately simulate modern-day absolute ozone concentrations (within ± 15%) over the 1971-2015 period.
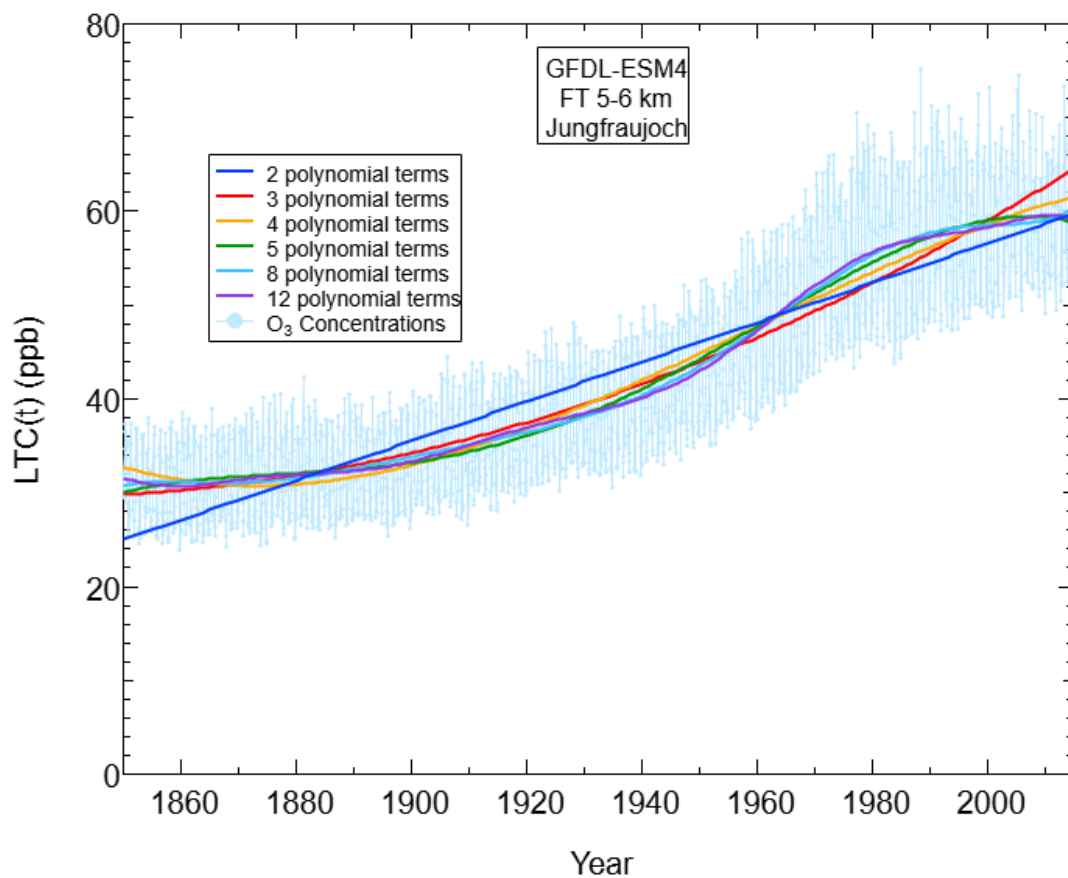
Figure S1. Comparison of LTC(t) derived from fits of polynomials of orders ranging from 1 (a straight line) to 11 (a 12-term polynomial fit), which overlay the example time series that is fit.

Table S1. Comparison of parameters of the fundamental term of Equation 4 derived from fits to the GFDL-ESM4 Jungfraujoch 5-6 km time series illustrated in Figure S1 with LTC(t) polynomial fits with varying number of terms. Table includes parameters defining both the preindustrial fundamental frequency (A_1 and ϕ_1) and the Gaussian function that describes the shift of the fundamental frequency (r, m, s, r_ϕ, m_ϕ, and s_ϕ), as well as the percentage of the variance in the original time series captured by the fit. We include one more significant figure than is statistically justified in the table entries to show the gradual improvement in the confidence limits of derived parameters.

Polynomial Terms	A_1	ϕ_1	r	m	s	r_ϕ	m_ϕ	s_ϕ	Variance Captured
2	5.87 ± 0.31 ppb	-0.602 ± 0.064 rad	4.03 ± 0.55 ppb	1982.8 ± 3.8	34.6 ± 6.8 years	35.3 ± 4.1 days	1991.2 ± 6.3	52 ± 12 years	92.8%
3	5.83 ± 0.23 ppb	-0.606 ± 0.046 rad	4.03 ± 0.40 ppb	1982.9 ± 2.9	36.2 ± 5.3 years	35.1 ± 3.0 days	1990.2 ± 4.6	50.0 ± 8.6 years	96.1%
4	5.82 ± 0.20 ppb	-0.607 ± 0.041 rad	4.04 ± 0.35 ppb	1982.8 ± 2.6	36.1 ± 4.6 years	35.1 ± 2.7 days	1990.8 ± 4.3	50.6 ± 7.9 years	97.0%
5	5.83 ± 0.18 ppb	-0.603 ± 0.037 rad	4.04 ± 0.31 ppb	1982.7 ±2.3	35.6 ± 4.1 years	35.3 ± 2.4 days	1991.4 ± 4.0	51.7 ± 7.3 years	97.6%
8	5.83 ± 0.17 ppb	-0.605 ± 0.035 rad	4.04 ± 0.30 ppb	1982.7 ± 2.2	35.9 ± 3.9 years	35.2 ± 2.3 days	1991.0 ± 3.7	51.1 ± 6.8 years	97.8%
12	5.83 ± 0.17 ppb	-0.604 ± 0.034 rad	4.04 ± 0.29 ppb	1982.7 ± 2.1	35.8 ± 3.8 years	35.3 ± 2.3 days	1991.3 ± 3.7	51.5 ± 6.8 years	97.9%

40
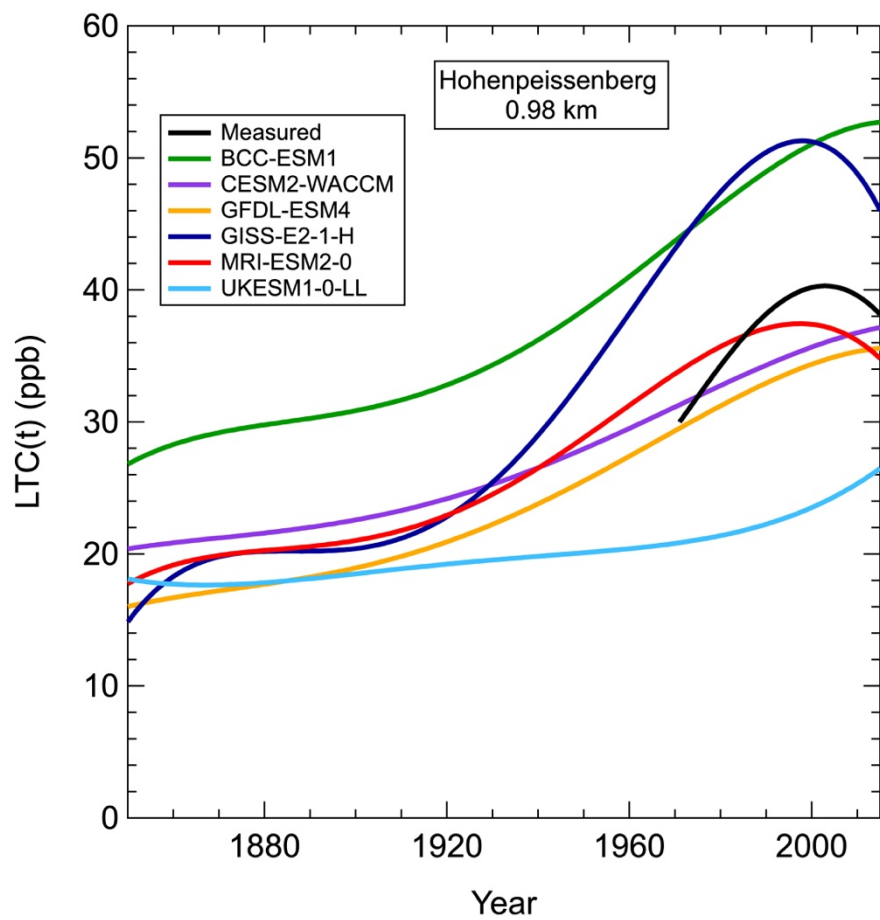
45   **Figure S2. Comparison of model- and measurement-based LTC(t) functions at Hohenpeissenberg derived from 5-term polynomial fits. LTC(t) represents the long-term average ozone concentrations underlying the monthly mean ozone time series.**

Text S2. Fourier Transform Analysis

Figure S3 shows Fourier transforms of the detrended ozone time series for all model simulations and locations. The Fourier transforms are calculated for 1850-1880, before the seasonal cycle began to shift, so they show harmonic amplitudes representative of the preindustrial seasonal cycle. These amplitudes match the amplitudes of the fundamental and second harmonic shown in Figures 3, S4 and S5. Among the different sites, there are similarities in the results of the Fourier analysis. First, the fundamental harmonic is typically larger than the second harmonic. Exceptions are the two lower-elevation North American sites, Lassen NP and Trinidad Head at 1 km, for which the first two harmonic frequencies are approximately equal in amplitude. It is important to note that when the seasonal cycle shifts take place, the fundamental amplitude grows so that it is larger than the second harmonic at all sites, even Lassen NP and Trinidad Head at 1 km. A second and more important similarity in the Fourier analysis is that together the fundamental and second harmonic frequencies capture most of the variance associated with the seasonal cycle. Harmonics higher than the second consistently make only smaller contributions across all locations and models; for most cases, higher harmonics are not statistically significant at the 95% confidence interval. Hence, we consider only the fundamental and second harmonic as the constituents of the seasonal cycle in our analysis.
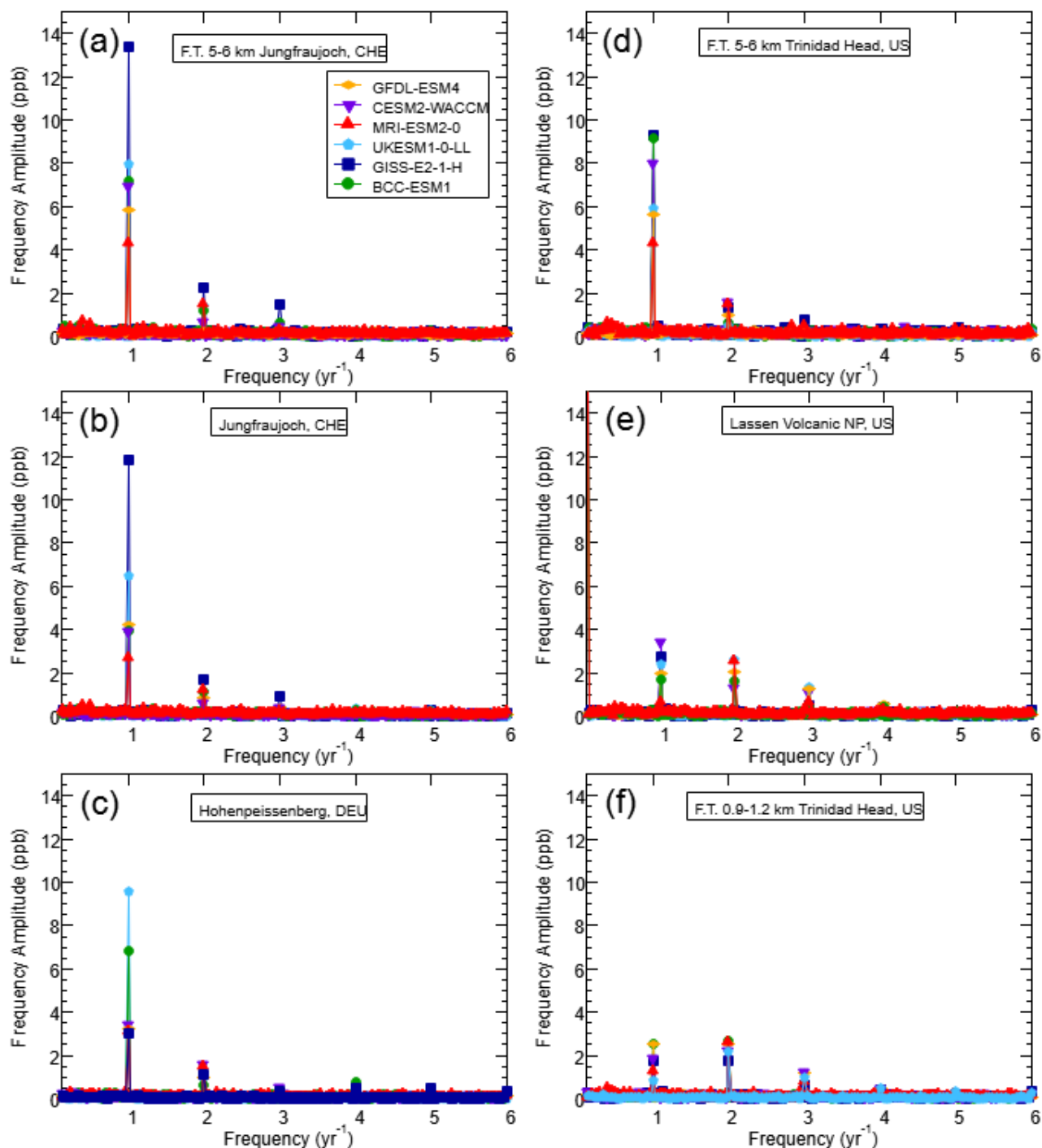
Figure S3. Fourier Transform of the detrended monthly means at all locations and model simulations considered. The horizontal axes show the frequency of the constituent sine functions that combine to form the overall seasonal cycle, and the vertical axes show their amplitudes. Panels (a), (b), and (c) show the European sites, and panels (d), (e), and (f) show the North American sites. The graphs are arranged from bottom to top in order of increasing location elevation.

65

Text S3. Preindustrial seasonal cycle at lower elevations

In the paper, we illustrate the preindustrial seasonal ozone cycle for the two free troposphere locations, as they are expected to be least influenced by continental influences, and thus most representative of the background troposphere. Here, we examine the preindustrial seasonal cycle for the four other, lower elevation locations included in our analysis, which are more influenced by surface emissions and ozone loss.

Figures S4 and S5 show plots similar to Figure 3 of the paper; they quantitatively examine the preindustrial seasonal cycle at the lower-elevation sites. There are two important takeaways from Figures S4 and S5. First, at the European sites (Jungfraujoch and Hohenpeissenberg), the preindustrial seasonal cycle is largely determined by the fundamental (which is larger in magnitude than higher-order frequencies) and reaches a maximum in the spring or early summer for most models. In contrast, the seasonal cycle at the North American sites (Lassen NP and Trinidad Head at 1 km) is more varied between models. Some models simulate a springtime ozone maximum and summertime minimum, and most models agree on a second harmonic with spring and autumn peaks, both of which are characteristics of ozone in the MBL (Parrish et al., 2016). Therefore, the lower-elevation North American sites are somewhat different in character from their European counterparts because they are more impacted by MBL conditions due to their near coastal locations than are the European sites, which are at more nearly mid-continental locations. Second, despite apparent MBL influence on the North American sites, the overall preindustrial seasonal cycle at low-elevation sites in both Europe and North America (panels (c) and (f) of Figures S4 and S5) is generally similar to the free tropospheric preindustrial seasonal cycle (panels (c) and (f) of Figure 3): in most models, the seasonal maximum occurs within spring or early summer, regardless of the relative contribution of certain harmonics or ozone levels during other parts of the year.
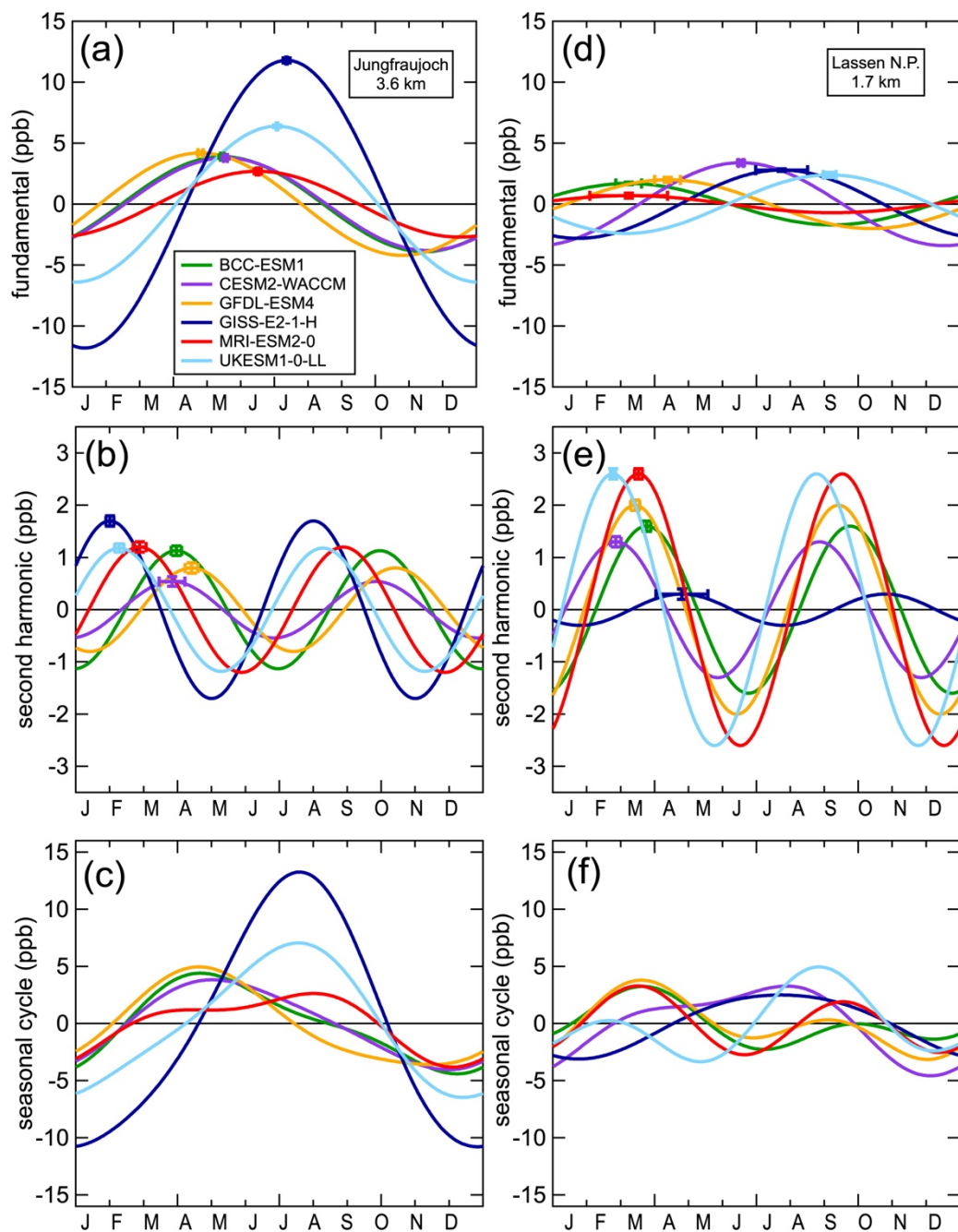
Figure S4. Harmonic analysis of preindustrial seasonal cycle at Jungfraujoch and Lassen NP. Figure is in the same format as Figure 3 of the manuscript.

90
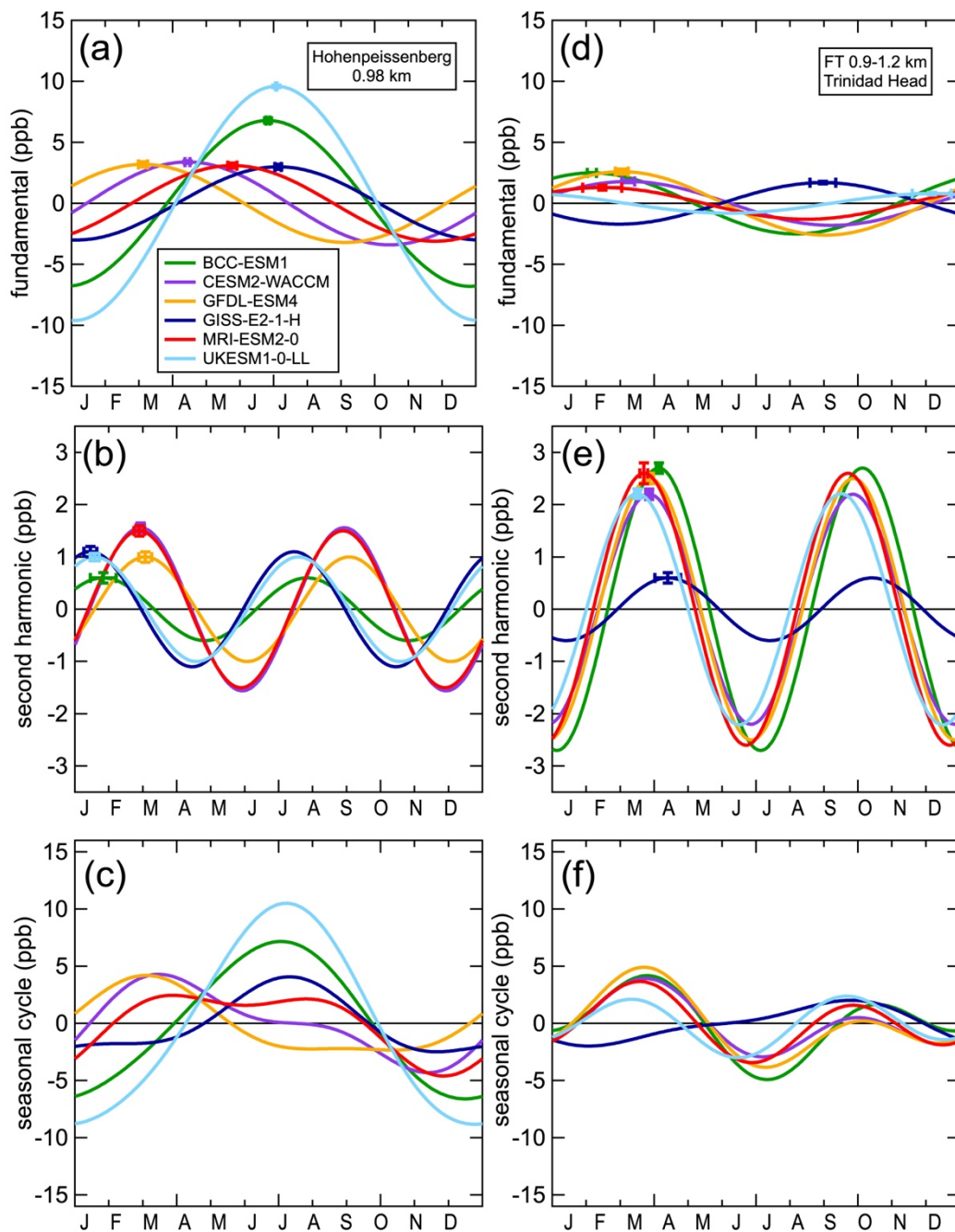
Figure S5. Harmonic analysis of preindustrial seasonal cycle at Hohenpeissenberg and Trinidad Head 0.9-1.2 km locations. Figure is in the same format as Figure 3 of the manuscript.

Text S4. Seasonal cycle shift in the FT 200 km west of US Coast

95   All of the measurements and model simulations considered in the manuscript are from European and North American continental locations. Here we compare model simulation results from 200 km west of Trinidad Head over the Pacific Ocean (Figure S6), a location more isolated from continental influences, with the continental locations. We take model results from the same two altitudes considered in the manuscript for Trinidad Head: one near the top of the MBL at ~1 km, and a second within the free troposphere between 5-6 km. We present this comparison because the coarse spatial resolution of the models

100   give grid cells that typically include 10^4 km^2; therefore, the model cell containing Trinidad Head, located on the west coast of California, includes both significant ocean and land areas. The offshore simulation results are expected to be more representative of the baseline troposphere without direct continental emissions. There are no measurements from this offshore location to compare with the model simulations.

Similar seasonal cycle shifts are seen in the free troposphere model simulations over the Pacific. The upper right graph in

105   Figure S6 compares the phase of the fundamental frequency in the free troposphere throughout the simulation time period at both locations; each of the six models simulates similar behaviour at the two sites. The amplitude of the fundamental in the free troposphere (upper left graph in Figure S6) also exhibits similar behaviour at both locations, although there are noticeable offsets in the magnitudes of the amplitudes. The similarity of the simulations at these two locations in the free troposphere again emphasizes that the shifts in the ozone seasonal cycle are common throughout the baseline troposphere at northern

110   midlatitudes.

At 1 km altitude the model simulations of the fundamental of the seasonal cycle are strikingly different between the continental and marine locations. It is likely that this altitude at the coastal location of Trinidad Head is particularly challenging for models to accurately simulate, since it represents both horizontal and vertical transitions – from the MBL to the free troposphere and from the marine to the continental environments. The contrasting behaviour shown in the lower panel of

115   Figure S6 emphasizes that the seasonal shift is driven by temporal changes in anthropogenic precursor emissions (see discuss in Section 3.4 of the paper) , which are primarily located at the continental surfaces, but the resulting seasonal shifts are seen throughout the troposphere.
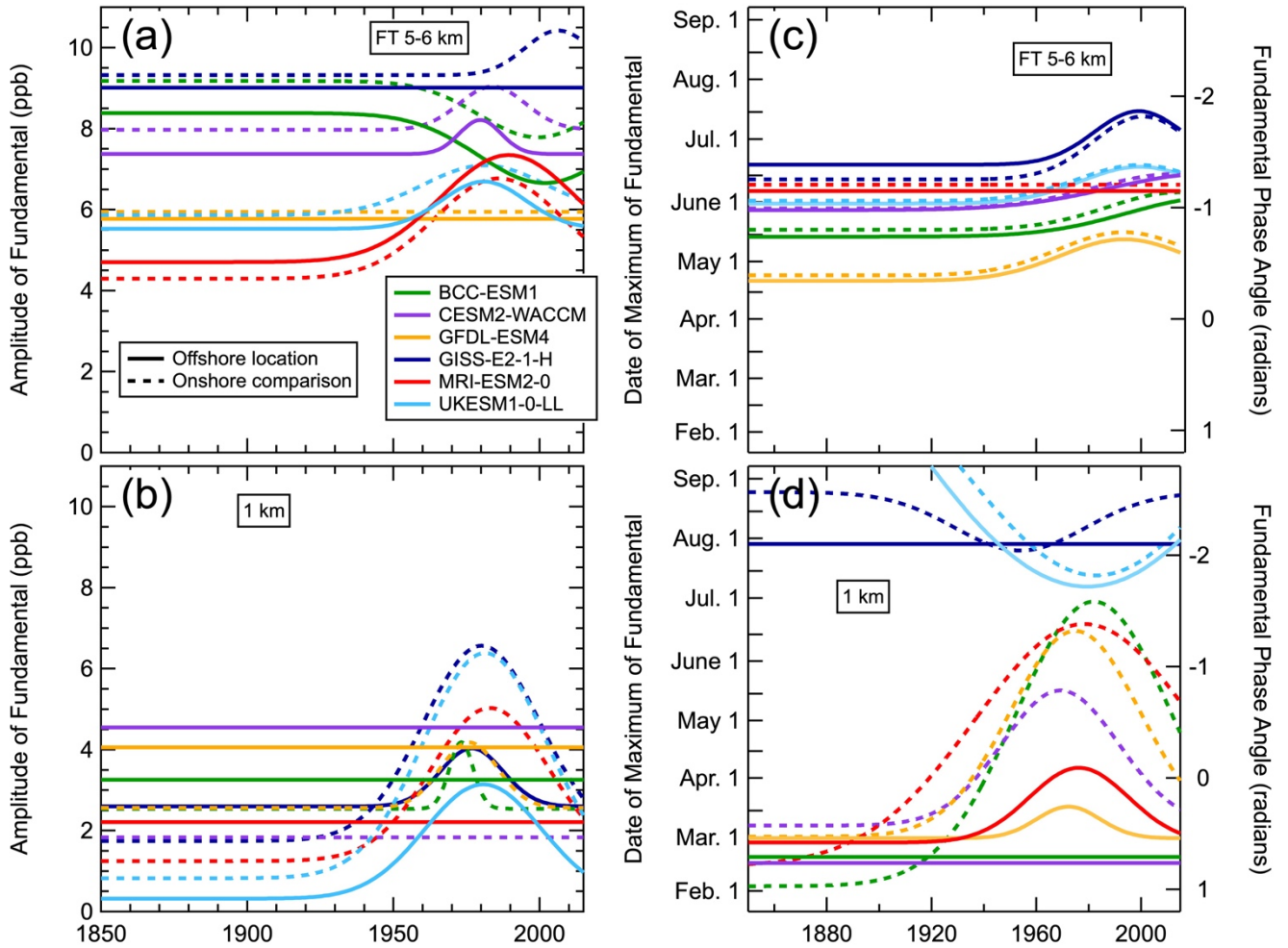
Figure S6. Comparison of the shift of the fundamental harmonic of the seasonal ozone cycle at Trinidad Head and at a location 200 km offshore to the west at the two indicated altitudes. The format and dashed curves are the same as the top and bottom panels of Figure 6 of the paper, except a greater range is included in the y axes in the right panel. Left and right panels quantify the amplitude and phase, respectively, of the fundamental as a function of year. The left axes in the right panels give the date of the seasonal maximum, while the right axes show corresponding values of the phase in radians. Colors identify the respective model simulations.

Text S5. Dominance of anthropogenic activity in emissions and seasonal cycles of emissions.

Anthropogenic activity is predominantly responsible for rising overall emissions in the latter half of the 20th Century. We consider the combined anthropogenic and biomass burning emissions; these are the emissions that are common between all models. While emissions from all sources influence ozone formation and can potentially cause shifts in the seasonal cycle, Figure S7 shows that biomass burning and natural emissions are approximately constant over time; it is anthropogenic emissions that substantially vary. This figure also emphasizes that anthropogenic activity makes a much larger contribution to overall emissions at northern midlatitudes than does biomass burning, especially after the mid-20th Century.

There is seasonal variation in anthropogenic and biomass burning emissions, as shown by the plot of monthly mean emissions in Figure S8; a seasonal cycle in emissions could potentially drive a seasonal cycle in ozone. The seasonal cycle amplitude of the NMVOC emissions (Figure S8a) decreases somewhat between 1850 and the late 20th Century. Beginning in about 1990, there are some months with abnormally high NMVOC emissions; this is attributed to the inclusion of satellite observations in determining wildfire emissions, which can have large month-to-month variability that is captured by the satellite data (Van Marle et al., 2017). The seasonal cycle of anthropogenic and biomass burning NOx (Figure S8b) does vary in amplitude; however, seasonal NOx variations are small (~ 5% of the total emissions) compared to the amplitude of the seasonal ozone cycle (which is between 20% and 40% of the ozone concentrations). It is not evident in Figure S8, but the phases of NOx and NMVOC emissions remain constant over the 1850-2014 period. Seasonal NMVOC emissions are at their highest in the summer (owing to summer wildfires), while seasonal NOx emissions peak in the winter, due to peak energy usage associated with heating buildings. We can find no close correlation between the seasonal cycles of the precursor emissions and that of ozone. Based on this analysis, we conclude that the seasonality of emissions is not related to the changing seasonal ozone cycle.
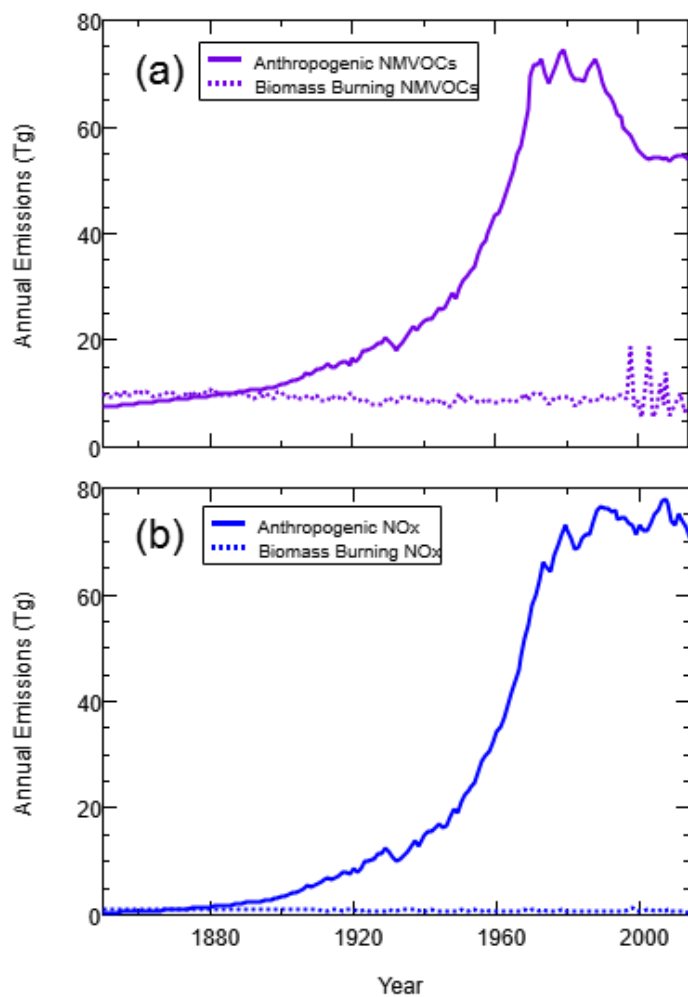
Figure S7. Comparison of emissions from anthropogenic and biomass burning sources for (a) NMVOCs and (b) NOx in units of mass of NO$_2$ emitted. For both species, anthropogenic emissions and biomass burning emissions are about equal in magnitude in 1850; however, by the mid-20th Century anthropogenic emissions begin rising rapidly while biomass burning emissions remain approximately constant.

150
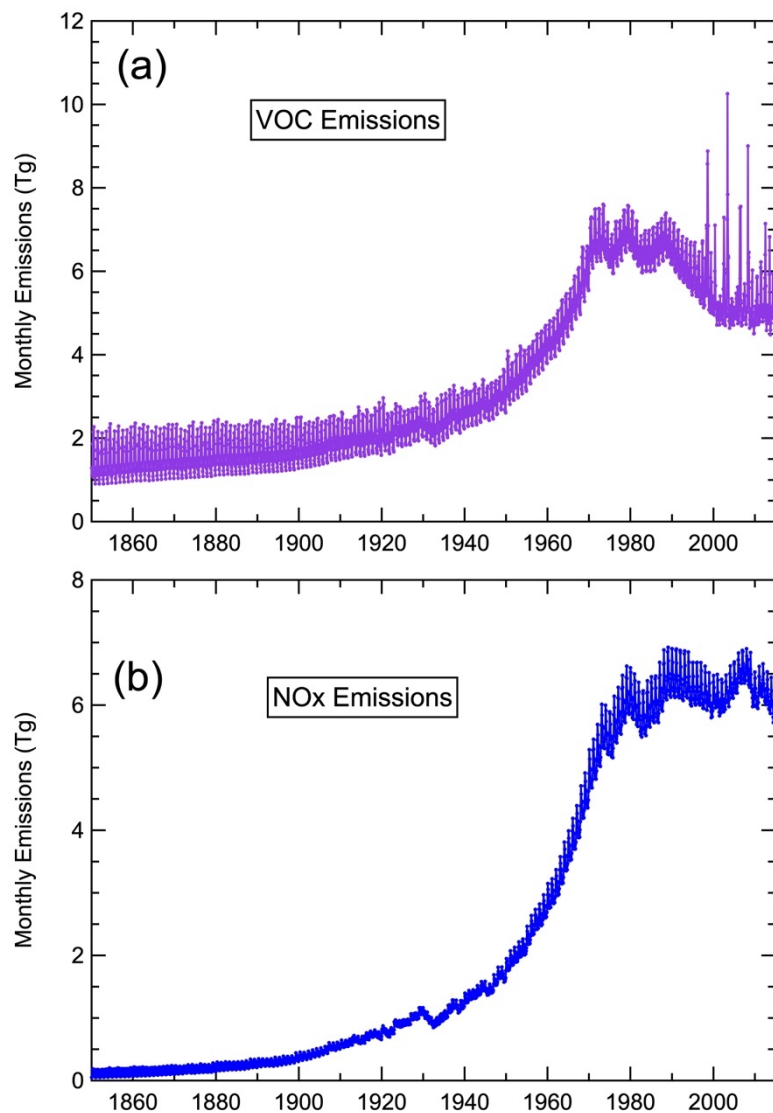
Figure S8. Monthly mean anthropogenic and biomass burning emissions for (a) VOC and (b) NOx in units of mass of NO₂ emitted.
155 **The seasonal cycle is represented by the spread of the points about the long-term change.**

Text S6. Model-specific natural emissions and methane

All models share the same emission inventories for anthropogenic and biomass burning emissions; these common emissions are detailed and analyzed in the paper. However, each model has unique parameterizations and physical processes that determine precursor emissions from natural sources, so natural emissions differ between models. Table S2 describes the natural sources of ozone precursor emissions in four models; and the emission totals integrated from 30° to 60° N are shown in Figure S9.

The VOC emissions are derived and apportioned between component species through different approaches, and are given in varying units. As a consequence, we cannot quantitatively compare either natural emissions with the anthropogenic and biomass burning emissions or the magnitude of natural VOC emissions between different models. Figure S9a shows natural VOC emissions from four models. Notably, the units in which they were specified vary; natural VOC emissions from GFDL-ESM4 are in units of mass of carbon emitted, while emissions from other models are in units of total VOC mass emitted. For example, the GISS-E2-1-H model specifies most natural emissions (DMS, isoprene, etc.) in total mass of emitted species, but emissions of entire families of compounds (e.g., alkenes) are given as moles of compounds. Therefore, Figure S9a gives only a qualitative comparison of natural VOC emissions between models and with the anthropogenic and biomass burning precursor emissions given in Figure 8 of the manuscript. Nevertheless, Figure S9a does indicate that natural VOC emissions are largely constant over time, which implies that anthropogenic emissions are primarily responsible for the seasonal cycle shifts.

Figure S9b shows natural NOx emissions, which include lightning and soil emissions. Natural NOx emissions are far smaller in magnitude than the anthropogenic and biomass burning NOx emissions given in Figure 8 of the manuscript, especially after the mid 20th Century. Figure S9b indicates that natural NOx emissions are nearly constant over time in contrast to the anthropogenic and biomass burning emissions, which again implies that anthropogenic emissions are primarily responsible for the seasonal cycle shifts.

Methane is treated differently from the other VOCs in the model simulations due to its much longer lifetime than other VOCs and its relatively uniform concentration in the troposphere. Figure S9c gives the time series of methane concentrations specified for northern midlatitudes for all of the ESMs. Methane concentrations approximately doubled between 1850 and 2015, with the most rapid increases between 1950 and 1990. Methane changes may also influence the seasonal cycle shift, but we do not attempt to quantitatively analyze that impact.

Table S2. Description of natural ozone precursor emissions by model.

Model	Natural NOx Emissions	Natural VOC Emissions	Comments
BCC-ESM1	Soil nitrification, lightning	Biogenic VOCs (see comment)	Biogenic emissions taken from the MOZART-2 standard package for the Atmospheric Chemistry and Climate Model Intercomparison Project (ACCMIP) emission inventory. (See Wu et al., 2020, for details.)
CESM2-WACCM	Soil nitrification, lightning	Biogenic VOCs and others (many species; see Emmons et al., 2020).	Full details of emissions given by Emmons et al. (2020)
GFDL-ESM4	Soil nitrification, lightning	Biogenic VOCs (isoprene, terpenes, ethane, propane, propene, ethanol, methanol, acetone, carbon monoxide), ocean sources (DMS, ammonia, ethane, propane, propene, carbon monoxide, hydrogen)	Biogenic isoprene and terpene emissions were calculated interactively using MEGAN; ocean emissions of DMS and NH_3 are calculated interactively; other natural emissions are prescribed. Many of the prescribed emissions were taken from the POET inventory. (See Horowitz et al., 2020, for details.)
GISS-E2-1-H	Soil nitrification, lightning	DMS (from ocean sources), Terpenes, Alkenes, Isoprene, Paraffin	Emission sources interactive within model. We examine initial conditions of 3 ensemble members; all produced statistically similar parameters.
MRI-ESM2-0	Soil nitrification, lightning	Biogenic VOCs (ethane, propane, ethene, propene, acetone, isoprene, and terpenes), ocean-based VOCs (ethane, propane, ethene, propene, acetone, and carbon monoxide)	MRI-ESM2-0 model includes 5 historical simulations. Lightning NOx is an interactive variable calculated in each simulation; all other emissions are constant.
UKESM1-0-LL	Soil nitrification, lightning	Biogenic VOCs (isoprene, ethane, propane, and formaldehyde), ocean-based VOCs (ethane, propane, and carbon monoxide)	UKESM1-0-LL model includes 5 historical simulations. Isoprene and lightning NOx are interactive variables calculated in each simulation, all other emissions are prescribed.

185
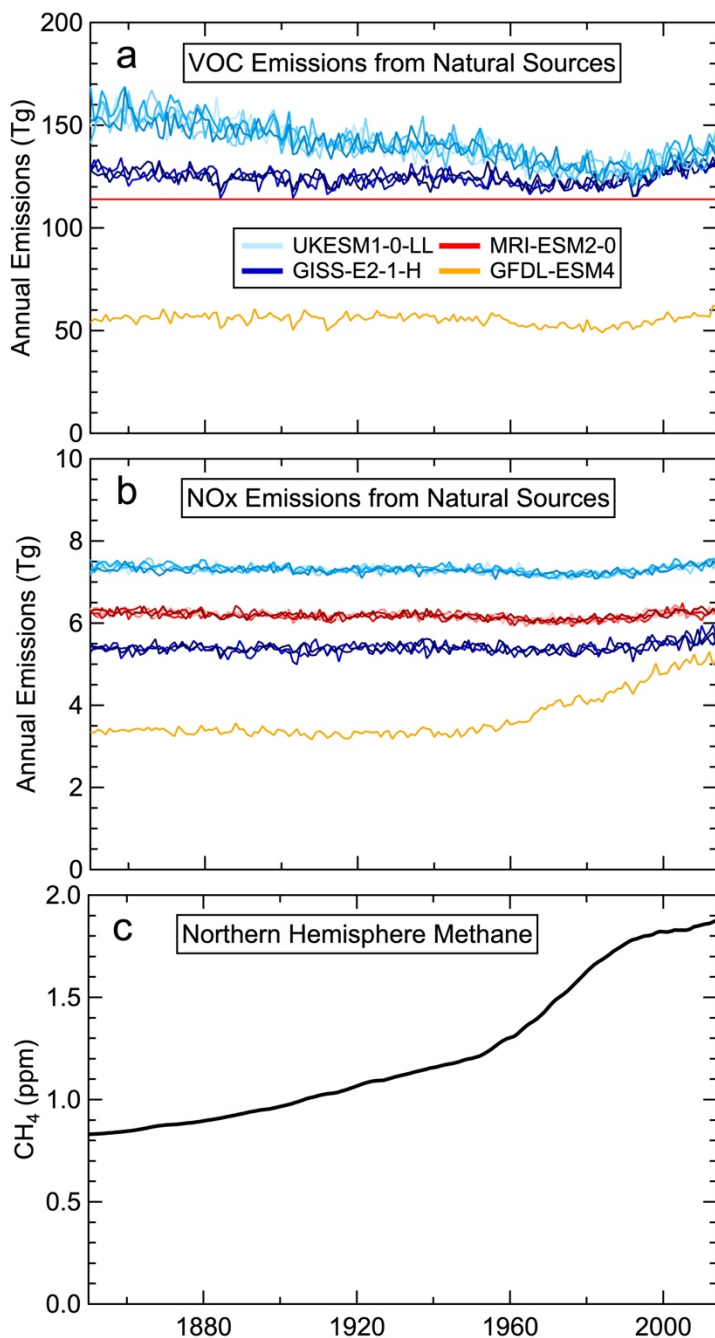
Figure S9. Natural emissions in CMIP6 models. Panels (a) and (b) show VOC and NOx emissions, and panel (c) shows methane concentrations across the northern hemisphere, which were common to all models. NOx emissions are given in mass of NO_2 emitted, but there is no common unit for VOC emissions; for GFDL-ESM4, units are mass C emitted, for GISS-E2-1-H, MRI-ESM2-0, and UKESM1-0-LL units are raw mass of VOCs emitted, with some exceptions as described in Section S6. Panels (a) and (b) include multiple ensembles for all models (except GFDL-ESM4), which are represented as similarly-colored traces that often overlap.

190

Table S3a. Gaussian parameters that define simulated seasonal ozone cycle shift over Europe. First two rows give weighted mean over all six model simulations at the three European locations. Positive r values for the phase shift indicate a seasonal cycle shifting towards a later annual maximum. The seasonal cycle Gaussian parameters are averaged over the three European locations.

Western Europe	Gaussian amplitude, r parameter	Gaussian maximum, m parameter (Year)	Width of Gaussian, s parameter (years)
Mean European Phase	14 ± 8 days	1985 ± 8	17 ± 17
Mean European Amplitude	2.9 ± 1.4 ppb	1990 ± 3	15 ± 9
BCC-ESM1 Phase	18 ± 2 days	1990 ± 2	29 ± 4
BCC-ESM1 Amplitude	4.7 ± 0.2 ppb	1986 ± 1	28 ± 1
CESM2-WACCM Phase	31 ± 2 days	1991 ± 1	35 ± 2
CESM2-WACCM Amplitude	5.0 ± 0.2 ppb	1987 ± 1	26 ± 1
GFDL-ESM4 Phase	52 ± 2 days	1986 ± 1	47 ± 2
GFDL-ESM4 Amplitude	5.2 ± 0.2 ppb	1985 ± 1	26 ± 1
GISS-E2-1-H Phase	11 ± 1 days	1999 ± 3	32 ± 5
GISS-E2-1-H Amplitude	6.7 ± 0.2 ppb	1987 ± 1	27 ± 1
MRI-ESM2-0 Phase[a]	29 ± 4 days	1994 ± 4	54 ± 11
MRI-ESM2-0 Amplitude	9.5 ± 0.2 ppb	1988 ± 1	34 ± 1
UKESM1-0-LL Phase[b]	12 ± 3 days	2020 ± 23	49 ± 20
UKESM1-0-LL Amplitude	7.1 ± 0.1 ppb	1990 ± 1	40 ± 1

[a] Results from Hohenpeissenberg, the only data set with statistically significant phase parameters

[b] Results from European free troposphere 5-6 km, the only data set with statistically significant phase parameters

Table S3b. Gaussian parameters that define simulated seasonal ozone cycle shift over North America. First two rows give weighted mean over all six model simulations at the three North American locations. Positive *r* values for the phase shift indicate a seasonal cycle shifting towards a later annual maximum. The seasonal cycle Gaussian parameters are averaged over the three North American locations.

North America	Gaussian amplitude, i.e., *r* parameter	Year of Gaussian maximum, i.e., *m* parameter	Width of Gaussian, i.e., *s* parameter (years)
Mean North American Phase	29 ± 1 days	1982 ± 1	40 ± 2
Mean North American Amplitude	3.7 ± 0.1 ppb	1989 ± 1	27 ± 1
BCC-ESM1 Phase	85 ± 4 days	1983 ± 2	43 ± 3
BCC-ESM1 Amplitude[a]	1.3 ± 0.2 ppb	1974 ± 1	13 ± 2
CESM2-WACCM Phase	17 ± 3 days	1972 ± 3	32 ± 5
CESM2-WACCM Amplitude[b]	2.6 ± 0.3 ppb	1976 ± 2	26 ± 3
GFDL-ESM4 Phase	52 ± 2 days	1986 ± 1	47 ± 2
GFDL-ESM4 Amplitude[c]	4.5 ± 0.3 ppb	1977 ± 1	28 ± 2
GISS-E2-1-H Phase	27 ± 2 days	1993 ± 3	28 ± 4
GISS-E2-1-H Amplitude	4.5 ± 0.2 ppb	1981 ± 1	30 ± 2
MRI-ESM2-0 Phase[d]	122 ± 15 days	1977 ± 3	59 ± 9
MRI-ESM2-0 Amplitude	3.3 ± 0.2 ppb	1983 ± 2	29 ± 3
UKESM1-0-LL Phase[e]	12 ± 2 days	1982 ± 1	51 ± 6
UKESM1-0-LL Amplitude	4.5 ± 0.2 ppb	1981 ± 1	32 ± 1

[a] In the free troposphere, the amplitude decreased rather than increased

[b] Includes results from two higher elevation locations; phase shift was not statistically significant at Trinidad Head 1 km location

[c] Includes results from two lower elevation locations; phase shift was not statistically significant at Trinidad Head 5-6 km location

[d] Includes results from two lower elevation sites, amplitude shift was not statistically significant at Trinidad Head 5-6 km location
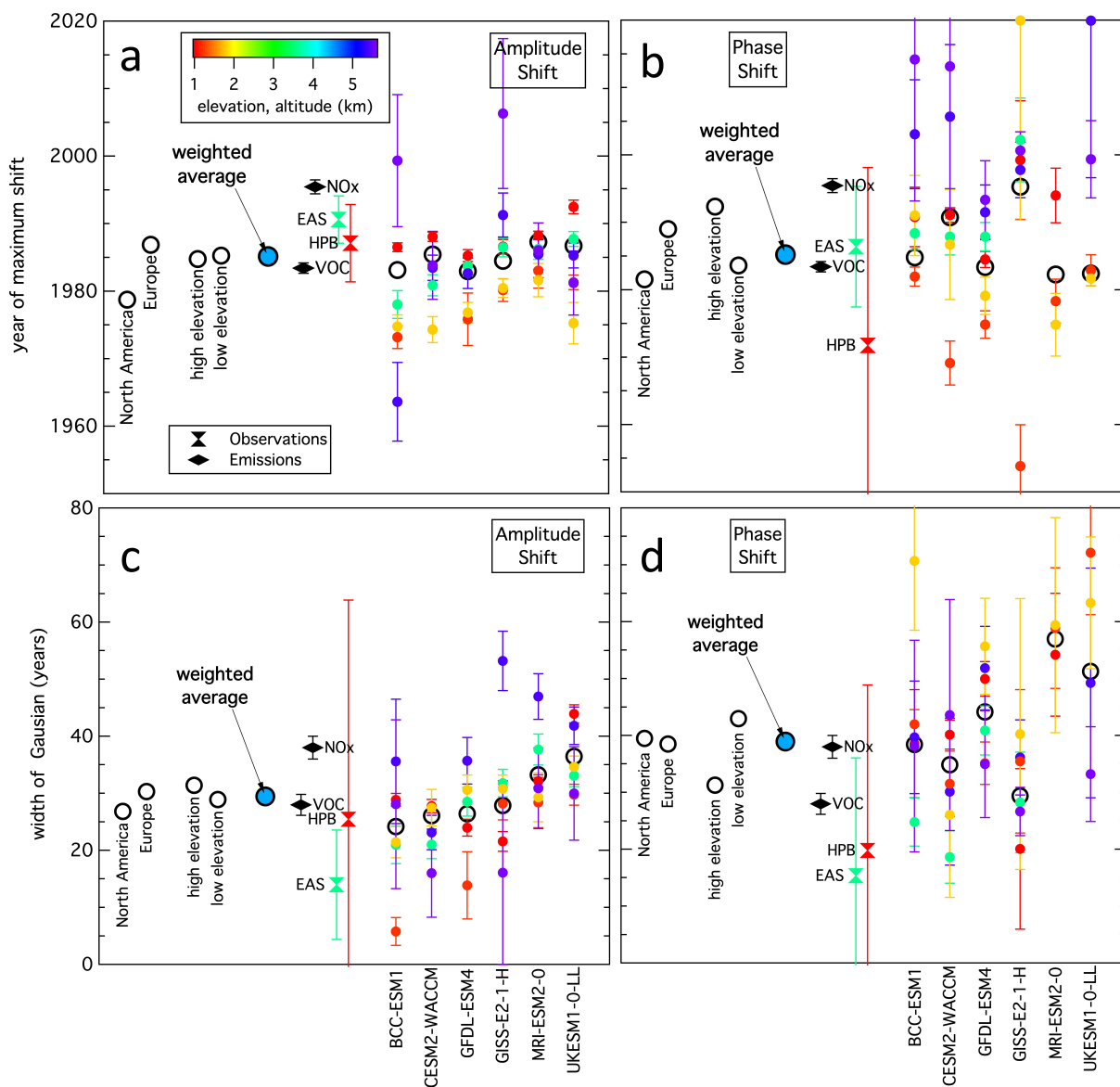
Figure S10. Results of ozone seasonal cycle shift analysis. The left and right graphs illustrate the shifts in the amplitude and phase of the seasonal cycle, respectively, for the year of maximum shift (a and b) and the half-width of the Gaussian function fit to the shifts (c and d). Small symbols with error bars are from fits to individual model results at individual locations; these are color-coded according to location elevation or altitude. Circles indicate weighted averages of the parameters derived in all fits: blue filled circle is the average for all six models at all six locations, the six-location averages for each model are to the right, and six-model averages for three locations selected for continent or elevation are to the left. Parameters with confidence limits derived from fits to observations at the European alpine sites (EAS) and Hohenpeissenberg (HPB) and VOC and NOx emissions are included near the center of each graph in the annotated symbols. This figure shows the respective panels of Figure 8 of the manuscript with compressed y-axes.

220
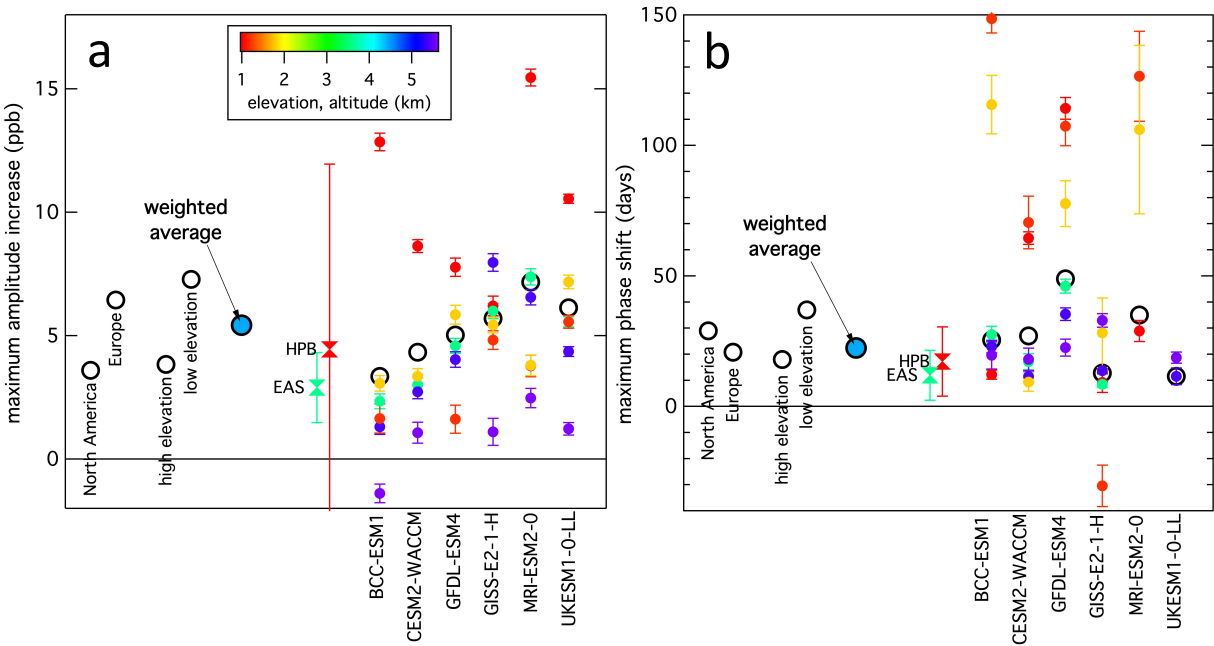
Figure S11. Results of ozone seasonal cycle shift analysis. Small symbols with error bars are from fits to individual model results at individual locations; these are color-coded according to location elevation or altitude. Circles indicate weighted averages of the
225 **parameters derived in all fits: blue filled circle is the average for all six models at all six locations, the six-location averages for each model are to the right, and six-model averages for three locations selected for continent or elevation are to the left. Parameters with confidence limits derived from fits to observations at the European alpine sites (EAS) and Hohenpeissenberg (HPB) are included near the center of each graph in the annotated symbols. This figure shows panels e) and f) of Figure 8 of the manuscript with compressed y-axes.**

230

Table S4. References for model descriptions and citations for the simulation results from the ESMs that participated in the CMIP6 exercise, and were used in this analysis.

Model	Reference	Data Citation
BCC-ESM1	Wu et al., 2019; 2020	Zhang et al., 2021
CESM2-WACCM	Emmons et al., 2020; Gettelman et al., 2019; Tilmes et al., 2019	Danabasoglu, 2019a; 2019b; 2019c
GFDL-ESM4	Dunne, 2020; Horowitz, 2020	Krasting et al., 2018
GISS-E2-1-H	Kelly et al., 2020	Miller et al., 2021.
MRI-ESM2-0	Yukimoto et al., 2019a; Oshima et al. 2020	Yukimoto et al., 2019b
UKESM1-0-LL	Sellar et al., 2019; Archibald et al., 2020	Good et al., 2019; Tang et al., 2019

References

235 Archibald, A. T., O'Connor, F. M., Abraham, N. L., Archer-Nicholls, S., Chipperfield, M. P., Dalvi, M., Folberth, G. A., Dennison, F., Dhomse, S. S., Griffiths, P. T., Hardacre, C., Hewitt, A. J., Hill, R. S., Johnson, C. E., Keeble, J., Köhler, M. O., Morgenstern, O., Mulcahy, J. P., Ordóñez, C., Pope, R. J., Rumbold, S. T., Russo, M. R., Savage, N. H., Sellar, A., Stringer, M., Turnock, S. T., Wild, O., and Zeng, G.: Description and evaluation of the UKCA stratosphere–troposphere chemistry scheme (StratTrop vn 1.0) implemented in UKESM1, Geosci. Model Dev., 13, 1223–1266,

240 https://doi.org/10.5194/gmd-13-1223-2020, 2020.

Danabasoglu, G.: NCAR CESM2-WACCM model output prepared for CMIP6 AerChemMIP, doi:10.22033/ESGF/CMIP6.10023, 2019a.

Danabasoglu, G.: NCAR CESM2-WACCM model output prepared for CMIP6 CMIP, doi:10.22033/ESGF/CMIP6.10024, 2019b.

245 Danabasoglu, G.: NCAR CESM2-WACCM model output prepared for CMIP6 ScenarioMIP, doi:10.22033/ESGF/CMIP6.10026, 2019c.

Dunne, J. P., Horowitz, L. W., Adcroft, A. J., Ginoux, P., Held, I. M., John, J. G., Krasting, J. P., Malyshev, S., Naik, V., Paulot, F., Shevliakova, E., Stock, C. A., Zadeh, N., Balaji, V., Blanton, C., Dunne, K.A., Dupuis, C., Durachta, J., Dussin, R., Gauthier, P. P. G., Griffies, S. M., Guo, H., Hallberg, R. W., Harrison, M., He, J., Hurlin, W., McHugh, C., Menzel,

250 R., Milly, P. C. D., Nikonov, S., Paynter, D. J., Ploshay, J., Radhakrishnan, A., Rand, K., Reichl, B. G., Robinson, T., Schwarzkopf, M. D., Sentman, L. A., Underwood, S., Vahlenkamp, H., Winton, M., Wittenberg, A. T., Wyman, B., Zeng,

Y., and Zhao, M.: The GFDL Earth System Model version 4.1 (GFDL-ESM4.1): Model description and simulation characteristics, submitted to Journal of Advances in Modeling Earth Systems, 2019MS002008, 2020.

Emmons, L. K., Orlando, J. J., Tyndall, G., Schwantes, R. H., Kinnison, D., Lamarque, J.-F., Marsh, D., Mills, M., Tilmes, S., Buchholtz, R. R., Gettelman, A., Garcia, R., Simpson, I., Blake, D. R. and Pétron, G.: The Chemistry Mechanism in the Community Earth System Model verson 2 (CESM2), J. Adv. Model. Earth Syst., 12, https://doi.org/10.1029/2019MS001882, 2020.

Gettelman, A., Mills, M. J., Kinnison, D. E., Garcia, R. R., Smith, A. K., Marsh, D. R., et al.: The whole atmosphere community climate model version 6 (WACCM6) J. Geophys. Res.: Atmos., 124. https://doi.org/10.1029/2019JD030943, 2019.

Good, P., Sellar, A., Tang, Y., Rumbold, S., Ellis, R., Kelley, D., Kuhlbrodt, T. and Walton, J.: MOHC UKESM1.0-LL model output prepared for CMIP6 ScenarioMIP, doi:10.22033/ESGF/790 CMIP6.1567, 2019.

Horowitz, L. W., Naik, V., Paulot, F., Ginoux, P. A., Dunne, J. P., Mao, J., Schnell, J., Chen, X., Lin, M., Lin, P., Malyshev, S., Paynter, D., Shevliakova, E., and Zhao, M.: The GFDL Global Atmospheric Chemistry-Climate Model AM4.1: Model Description and Simulation Characteristics, Journal of Advances in Modeling Earth Systems, 12, https://doi.org/10.1029/2019MS002032, 2020.

Kelley, M., G.A. Schmidt, L. Nazarenko, S.E. Bauer, R. Ruedy, G.L. Russell, A.S. Ackerman, I. Aleinov, M. Bauer, R. Bleck, V. Canuto, G. Cesana, Y. Cheng, T.L. Clune, B.I. Cook, C.A. Cruz, A.D. Del Genio, G.S. Elsaesser, G. Faluvegi, N.Y. Kiang, D. Kim, A.A. Lacis, A. Leboissetier, A.N. LeGrande, K.K. Lo, J. Marshall, E.E. Matthews, S. McDermid, K. Mezuman, R.L. Miller, L.T. Murray, V. Oinas, C. Orbe, C. Pérez García-Pando, J.P. Perlwitz, M.J. Puma, D. Rind, A. Romanou, D.T. Shindell, S. Sun, N. Tausnev, K. Tsigaridis, G. Tselioudis, E. Weng, J. Wu, and M.-S. Yao: GISS-E2.1: Configurations and climatology, J. Adv. Model. Earth Syst., 12, no. 8, e2019MS002025, doi:10.1029/2019MS002025, 2020.

Krasting, J. P., John, J. G., Blanton, C., McHugh, C., Nikonov, S., Radhakrishnan, A., Rand, K., Zadeh, N. T., Balaji, V., Durachta, J., Dupuis, C., Menzel, R., Robinson, T., Underwood, S., Vahlenkamp, H., Dunne, K. A., Gauthier, P. P. G., Ginoux, P., Griffies, S. M., Hallberg, R., Harrison, M., Hurlin, W., Malyshev, S., Naik, V., Paulot, F., Paynter, D. J., Ploshay, J., Schwarzkopf, D. 830 M., Seman, C. J., Silvers, L., Wyman, B., Zeng, Y., Adcroft, A., Dunne, J. P., Guo, H., Held, I. M., Horowitz, L. W., Milly, P. C. D., Shevliakova, E., Stock, C., Winton, M. and Zhao, M.: NOAA-GFDL GFDL-ESM4 model output prepared for CMIP6 CMIP. Version 20190727. Earth System Grid Federation. https://doi.org/10.22033/ESGF/CMIP6.1407, 2018.

Miller, R.L., G.A. Schmidt, L. Nazarenko, S.E. Bauer, M. Kelley, R. Ruedy, G.L. Russell, A. Ackerman, I. Aleinov, M. Bauer, R. Bleck, V. Canuto, G. Cesana, Y. Cheng, T.L. Clune, B. Cook, C.A. Cruz, A.D. Del Genio, G.S. Elsaesser, G. Faluvegi, N.Y. Kiang, D. Kim, A.A. Lacis, A. Leboissetier, A.N. LeGrande, K.K. Lo, J. Marshall, E.E. Matthews, S. McDermid, K. Mezuman, L.T. Murray, V. Oinas, C. Orbe, C. Pérez García-Pando, J.P. Perlwitz, M.J. Puma, D. Rind, A. Romanou, D.T. Shindell, S. Sun, N. Tausnev, K. Tsigaridis, G. Tselioudis, E. Weng, J. Wu, and M.-S. Yao: CMIP6

285   historical simulations (1850-2014) with GISS-E2.1. J. Adv. Model. Earth Syst., 13, no. 1, e2019MS002034, doi:10.1029/2019MS002034, 2021.

Oshima, N., Yukimoto, S., Deushi, M., Koshiro, T., Kawai, H., Tanaka, T. Y., and Yoshida, K.: Global and Arctic effective radiative forcing of anthropogenic gases and aerosols in MRI-ESM2.0, Prog. Earth Planet. Sc., 7, 38, https://doi.org/10.1186/s40645-020-00348-w, 2020.

290   Sellar, A. A., Jones, C. G., Mulcahy, J., Tang, Y., Yool, A., Wiltshire, A., O'Connor, F. M., Stringer, M., Hill, R., Palmieri, J., Woodward, S., Mora, L., Kuhlbrodt, T., Rumbold, S., Kelley, D. I., Ellis, R., Johnson, C. E., Walton, J., Abraham, N. L., Andrews, M. B., Andrews, T., Archibald, A. T., Berthou, S., Burke, E., Blockley, E., Carslaw, K., Dalvi, M., Edwards, J., Folberth, G. A., Gedney, N., Griffiths, P. T., Harper, A. B., Hendry, M. A., Hewitt, A. J., Johnson, B., Jones, A., Jones, C. D., Keeble, J., Liddicoat, S., Morgenstern, O., Parker, R. J., Predoi, V., Robertson, E., Siahaan, A., Smith, R. S.,
295   Swaminathan, R., Woodhouse, M. T., Zeng, G. and Zerroukat, M.: UKESM1: Description and evaluation of the UK Earth System Model, J. Adv. Model. Earth Syst., 2019MS001739, doi:10.1029/2019MS001739, 2019.

Tang, Y., Rumbold, S., Ellis, R., Kelley, D., Mulcahy, J., Sellar, A., Walton, J. and Jones, C.: MOHC UKESM1.0-LL model output prepared for CMIP6 CMIP, doi:10.22033/ESGF/CMIP6.1569, 2019.

Tilmes, S., Hodzic, A., Emmons, L. K., Mills, M. J., Gettelman, A., Kinnison, D. E., Park, M., Lamarque, J. -F., Vitt, F.,
300   Shrivastava, M., Campuzano Jost, P., Jimenez, J. and Liu, X.: Climate forcing and trends of organic aerosols in the Community Earth System Model (CESM2), J. Adv. Model. Earth Syst., 2019MS001827, doi:10.1029/2019MS001827, 2019.

Wu, T., Lu, Y., Fang, Y., Xin, X., Li, L., Li, W., Jie, W., Zhang, J., Liu, Y., Zhang, L., Zhang, F., Zhang, Y., Wu, F., Li, J., Chu, M., Wang, Z., Shi, X., Liu, X., Wei, M., Huang, A., Zhang, Y. and Liu, X.: The Beijing Climate Center Climate
305   System Model (BCC-CSM): the main progress from CMIP5 to CMIP6, Geosci. Model Dev., 12(4), 1573–1600, doi:10.5194/gmd-12-1573-2019, 2019.

Wu, T., Zhang, F., Zhang, J., Jie, W., Zhang, Y., Wu, F., Li, L., Yan, J., Liu, X., Lu, X., Tan, H., Zhang, L., Wang, J. and Hu, A.: Beijing Climate Center Earth System Model version 1 (BCC-ESM1): Model Description and Evaluation of Aerosol Simulations, Geosci. Model Dev., 13, 977–1005, doi:10.5194/gmd-13-977-2020, 2020.

310   Yukimoto, S., Kawai, H., Koshiro, T., Oshima, N., Yoshida, K., Urakawa, S., Tsujino, H., Deushi, M., Tanaka, T., Hosaka, M., Yabu, S., Yoshimura, H., Shindo, E., Mizuta, R., Obata, A., Adachi, Y., and Ishii, M.: The Meteorological Research Institute Earth System Model version 2.0, MRI-ESM2.0: Description and basic evaluation of the physical component. J. Meteor. Soc. Japan, 97, 931–965, doi:10.2151/jmsj.2019-051, 2019a.

Yukimoto, S., Koshiro, T., Kawai, H., Oshima, N., Yoshida, K., Urakawa, S., Tsujino, H., Deushi, M., Tanaka, T., Hosaka,
315   M., Yabu, S., Yoshimura, H., Shindo, E., Mizuta, R., Obata, A., Adachi, Y., and Ishii, M.: MRI MRI-ESM2.0 model output prepared for CMIP6 CMIP historical, Earth System Grid Federation, doi:10.22033/ESGF/CMIP6.6842, 2019b.

Zhang, J., Wu, T., Zhang, F. et al.: BCC-ESM1 Model Datasets for the CMIP6 Aerosol Chemistry Model Intercomparison Project (AerChemMIP). Adv. Atmos. Sci. 38, 317–328, https://doi.org/10.1007/s00376-020-0151-2, 2021.